Science Bulletin 63 (2018) 683–690

Contents lists available at ScienceDirect

Science Bulletin

journal homepage: www.elsevier.com/locate/scib

Article

Enhancing photocatalytic performance by constructing ultrafine TiO_2 nanorods/g-C_3N_4 nanosheets heterojunction for water treatment

Shiliang Luan [a], Dan Qu [a,*], Li An [a], Wenshuai Jiang [a], Xiang Gao [b,c], Shixin Hua [a], Xiang Miao [b,c], Yuanjing Wen [a], Zaicheng Sun [a,*]

[a] *Beijing Key Laboratory for Green Catalysis and Separation, Department of Chemistry and Chemical Engineering, School of Environmental and Energy Engineering, Beijing University of Technology, Beijing 100124, China*
[b] *State Key Laboratory of Luminescence and Applications, Changchun Institute of Optics, Fine Mechanics and Physics, Chinese Academy of Sciences, Changchun 130033, China*
[c] *University of Chinese Academy of Sciences, Beijing 100049, China*

ARTICLE INFO

Article history:
Received 11 February 2018
Received in revised form 22 March 2018
Accepted 2 April 2018
Available online 12 April 2018

Keywords:
Heterojunction
Photocatalyst
TiO_2 nanorods
g-C_3N_4 nanosheets
Water treatment

ABSTRACT

Photocatalysis is considered to be a clean, green and efficient method to purify water. In this report, we first developed a highly efficient ultrafine TiO_2 nanorods/g-C_3N_4 nanosheets (TiO_2 NR/CN NS) composites via a simple hydrothermal method. Tiny TiO_2 nanorods (diameter: ~1.5 nm and length: ~8.3 nm) were first loaded in situ on the CN NS by adding graphitic carbon nitride (g-C_3N_4) to the reaction solution. The TiO_2 NR/CN NS composites present high charge separation efficiency and broader light absorbance than P25 TiO_2. Furthermore, we illustrate that the TiO_2 NR/CN NS catalyst possesses high performance for the photocatalytic degradation of the common and stubborn pollutants in water, such as the rhodamine B (RhB) dye and phenol. Under visible light ($\lambda > 420$ nm) irradiation, the apparent rate of the TiO_2 NR/CN NR is 172 and 41 times higher than that of the P25 TiO_2 and TiO_2 NR, respectively. Additionally, we speculated that the heterojunction formed between TiO_2 NR and CN NS, which is the basis for the experiments we have designed and the corresponding results. We demonstrated that reactive oxidative species such as superoxide anion radical and holes play critical roles in the degradation, and the hydroxyl radical contributes nothing to the degradation.

1. Introduction

Considering the growing environmental issues worldwide, particularly water pollution, an increasing amount of research has been conducted to explore effective methods of water purification. Clean technology is emerging as a favorite direction, as it is well known that highly efficient photocatalyst can promote the direct conversion of solar energy to chemical energy and decontamination [1–5]. As one of the most typical photocatalysts, P25 TiO_2 has been extensively employed in the fields of solar fuel and sunlight-driven pollutant decomposition because of its strong oxidizing capability; high thermal, chemical and photostability; low cost; and nontoxicity [6,7]. However, it suffers from a narrow light absorption range and rapid charge recombination [2,8–10]. Constructing a heterojunction is an effective way to broaden the light absorption and promote the charge separation [11–13]. A well-known graphitic carbon nitride (g-C_3N_4) nanosheets (CN NS) has been developed as a novel metal-free photocatalyst owing to its visible light driven bandgap (~2.7 eV) and suitable band edge position for H_2 production and degradation of organic compounds [14–16]. Like various other photocatalysts, the efficiency of two-dimensional (2D) g-C_3N_4 is also limited by its high recombination rate of photogenerated electron-hole pairs [17,18]. Additionally, the band edge positions match with those of TiO_2, which provides an opportunity to fabricate the TiO_2/g-C_3N_4 heterojunction. Various strategies have been proposed to construct a TiO_2/g-C_3N_4 heterojunction by hydrothermal [19,20], calcination [21–23] and biomimetic [24].

Because photocatalytic water treatment is a heterogeneous reaction at the liquid-solid interface, the surface area and reactive site are critical factors for the catalytic reaction. Compared with bulk materials, a smaller sized catalyst yields a larger surface area and more active sites, the larger the surface area and the more active sites there are. However, the size of the catalyst is in nanometer scale, and it increases the difficulty of the separation of catalyst from the reaction solution, which results in secondary pollution. Therefore, new types of the photocatalyst are urgently needed that possess a high surfacearea and are easily recycled from the system. Herein, ultrafine TiO_2 nanorods (TiO_2 NRs) with a

---

* Corresponding authors.
E-mail addresses: qudanhappy@163.com (D. Qu), sunzc@bjut.edu.cn (Z. Sun).

https://doi.org/10.1016/j.scib.2018.04.002

diameter of ~1.5 nm and length of ~8.3 nm can be prepared from the solvothermal reaction of $TiCl_3$ and $SnCl_4$ in ethanol at 100 °C. The ultrafine TiO_2 nanorods were successfully loaded on the g-C_3N_4 nanosheets, forming the TiO_2 NR/g-C_3N_4 heterojunction by introducing the g-C_3N_4 nanosheets into the reaction solution. Scanning electron microscope (SEM) and transmission electron microscopy (TEM) images disclosed that the TiO_2 nanorods were highly dispersed on the surface of CN NR. UV–vis spectra show that the light absorption range extends into the visible light region. The photoluminescence (PL) spectra, photocurrent response, and electrochemical impedance spectroscopy (EIS) disclose a higher charge separation efficiency for the heterojunction photocatalyst than the single component. The new and ultrafine TiO_2 NR/CN NS composite exhibits good performance for removing pollutants in the water. When considering the performance of the photocatalytic degradation of rhodamine B (RhB) and phenol, the apparent degradation rate of the heterojunction of TiO_2 NR/CN NR is 172 and 7 times higher than that of the P25 TiO_2, respectively.

2. Materials and methods

2.1. Synthetic procedures

2.1.1. Preparation of TiO_2 NR catalysts

An aqueous solution of $TiCl_3$ (~15%, 2 mL) and $SnCl_4$ (0.5 mo/L, 2 mL) were mixed in ethanol (60 mL) and stirred for 3 h at room temperature. After being sealed with the polyethylene (PE) membrane, the reaction mixture was heated at 90 °C in an oven for 3 h. The TiO_2 NRs were collected by decanting the supernatant ethanol.

2.1.2. Preparation of g-C_3N_4 nanosheets

Bulk g-C_3N_4 was synthesized by heating 50 g of urea at 550 °C in a muffle furnace for 3 h (heating rate: 0.5 °C/min). Then, yellow bulk g-C_3N_4 nanosheets were obtained.

2.1.3. Preparation of TiO_2 NR/CN NS catalysts

TiO_2 NR/CN NS catalysts with different amount of CN NS (90, 120, 150 mg) were synthesized in the above TiO_2 NR synthesis reaction solution and denoted as TiO_2 NR/CN NS-1, 2, 3, respectively. Typically, the procedure for synthesizing the TiO_2 NR/CN NS catalyst with 120 mg g-C_3N_4 is described as follows: 120 mg CN NS was added into 60 mL ethanol and subjected to ultrasound for approximately 3 h. Then, aqueous $TiCl_3$ (~15%, 2 mL) and $SnCl_4$ (0.5 mol/L, 2 mL) were added to the above solution, which was stirred for 3 h at room temperature. The final mixture was transferred into the Teflon-lined stainless steel autoclave (100 mL) and maintained at 90 °C for 3 h. The resultant products were washed thoroughly with distilled water and ethanol three times and dried at 60 °C for 12 h.

2.2. Characterizations

The crystal structure of the samples was investigated using X-ray diffraction (XRD, Bruker D8 Advance X-ray diffractometer) with Cu Kα radiation ($\lambda = 0.15406$ nm) as the incident beam at 40 kV and 40 mA. The morphology of the samples was examined by TEM (FEI Tecnai G2 F20) operated at 200 kV and scanning electron microscope (SEM, JEOL S-4800) operated at 10 kV. UV–vis diffuse reflection spectroscopy (DRS) was performed with a Shimadzu UV-2600 spectrophotometer using $BaSO_4$ as the reference. The PL spectra of the photocatalysts were obtained a Hitachi F-7000 spectrometer with an excitation wavelength of 320 nm. The Brunauer-Emmett-Teller (BET) specific surface area was measured using a Quantachrome Surface Area and Pore Size Analyzer (Quantachrome Instrument version 3.01).

2.3. Photoelectrochemical measurement

Electrochemical measurements were obtained with an Autolab PGSTAT302N potentiostat/galvanostat in a conventional three-electrode cell. The carbon electrode was chosen as the counter electrode, the Ag/AgCl electrode was chosen as the reference electrode and the working electrode was prepared on the fluorine-doped tin oxide (FTO) glass. The sample (50 mg) was dispersed in a 100 mL I_2/acetone solution (0.5 mg/mL). A two-electrode process was used to deposit the samples at the applied potential of 10 V for 1 min. FTO glass substrates with a coated area about 1.5 cm × 1.5 cm were used for both electrodes. Then, the deposited electrodes were heated at 300 °C for 120 min to remove the residual I_2.

2.4. EIS measurement

EIS was performed using an electrochemical workstation (Autolab PGSTAT302N). The three-electrode cell was applied with a 0.1 mol/L Na_2SO_4 aqueous solution as the electrolyte that acted as the counter electrode, and Ag/AgCl acted as the reference electrode. The TiO_2 NRs, CN NSs, TiO_2 NR/CN NS-2 were electrodeposited on FTO glass and used as the working electrodes. The 300 W Xe lamp (AM 1.5) was adopted as the visible light source. EIS was measured over a range from 0.01 to 100 kHz with an amplitude of 0.02 V under an open-circuit potential and visible-light irradiation.

2.5. Total organic carbon (TOC) and high-performance liquid chromatography (HPLC) analysis

A 50 mg TiO_2 NR/CN NS-2 was suspended in phenol (30 mg/L) aqueous solution (100 mL) under vigorous stirring. The photocatalytic test was conducted with 300 W Xe lamp emitting full spectrum light for irradiation. The temperature of the reactant solution was maintained at 25 °C by a flow of cycle cooling water during the reaction.

3. Results and discussion

The CN NS were prepared using the high-temperature pyrolysis, starting from room temperature and increasing to 550 °C at 0.5 °C/min in muffle furnace. The urea was initially melted into a liquid and then produced ammonia, cyanamide, dicyandiamide, melamine, and others, and finally polymerized into g-C_3N_4 while a portion of small molecules would vaporized in the reaction. This process resulted in the high porous nanostructure and characteristic nanosheet morphology for the obtained g-C_3N_4. Fig. 1a shows the SEM images of g-C_3N_4. Ultrathin flake morphologies are observed in the as-prepared g-C_3N_4. TiO_2, as the highly active photocatalyst, has been extensively applied to photodecomposition of organic compounds due to the oxidative species that can be produced under UV light irradiation. The photocatalytic activity strongly depends on the surface capping groups and size. Wang's group [25] reported ultrafine TiO_2 nanocrystals with a clean surface that provide a potential opportunity to develop highly active photocatalyst. Fig. 1b and c show TEM and high-resolution TEM (HR-TEM) images of the TiO_2 NRs that were synthesized using a modified Wang's route [25]. The as-synthesized TiO_2 exhibits the morphology of tiny nanorods that are (1.5 ± 0.5) nm in diameter and (8.0 ± 2.0) nm in length. This ultrafine nanocrystal will provide a high surface area and highly active sites. The HR-TEM image shows a lattice fringe spacing of 3.20 Å, corresponding to the (1 1 0) facet of the rutile TiO_2. The TiO_2 NR/CN NS composites are

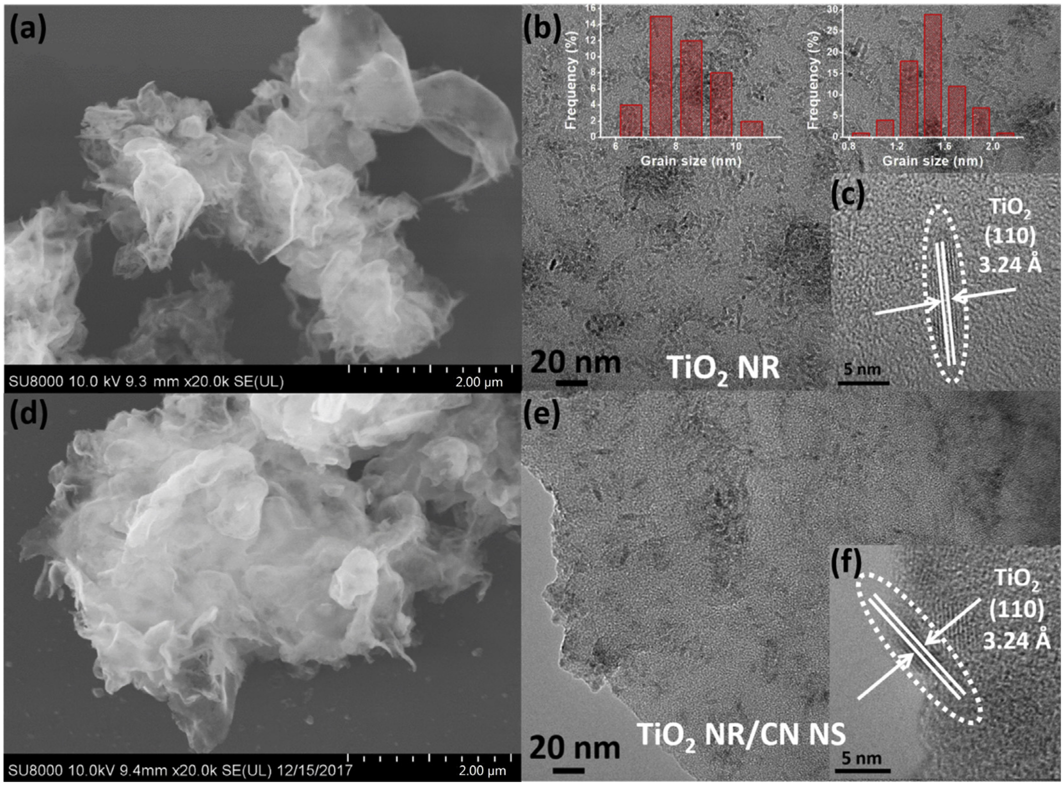

Fig. 1. (Color online) The morphologies of g-C_3N_4 nanosheets, TiO_2 NR, and TiO_2 NR/CN NS-2 composites. SEM images of g-C_3N_4 nanosheets (a) and TiO_2 NR/CN NS-2 composites (b); TEM and high resolution TEM (HR-TEM) images of TiO_2 NR (c, d) and TiO_2 NR/CN NS-2 composites (e, f).

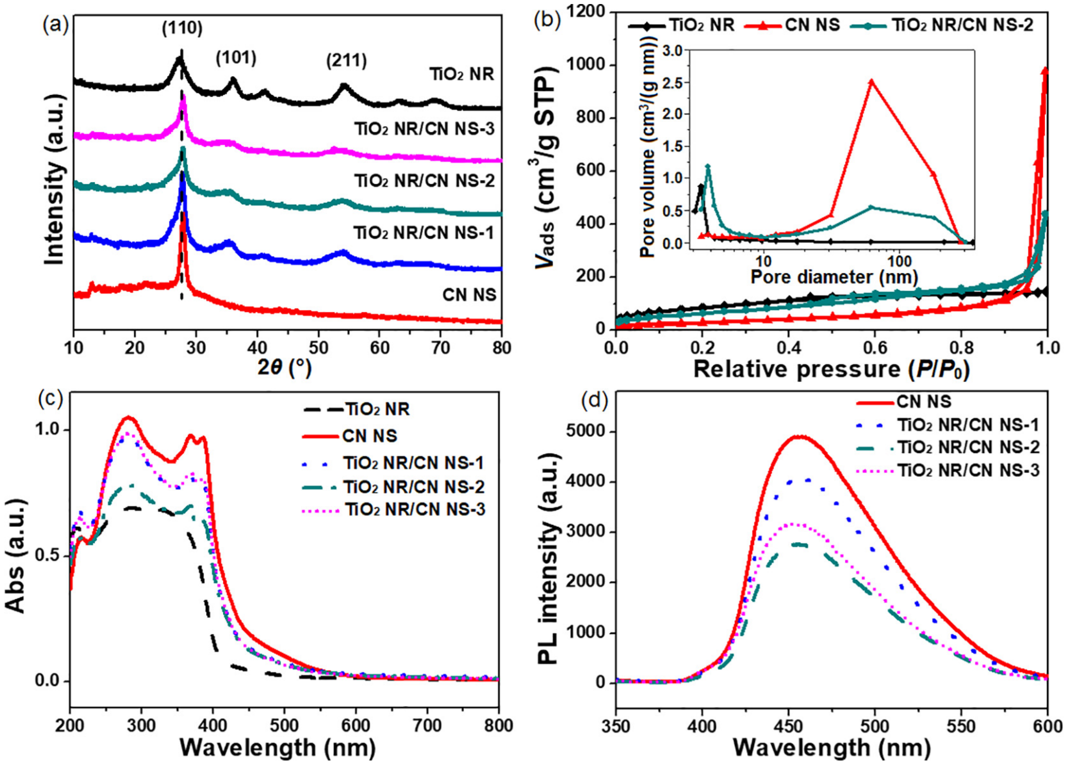

Fig. 2. (Color online) (a) XRD pattern of TiO_2 NR, CN NS and TiO_2 NR/CN NS composites. (b) Nitrogen sorption porosimetry studies of TiO_2 NR, CN NS and TiO_2 NR/CN NS-2 composites. (c) DRS UV–vis spectra of TiO_2 NR, CN NS and TiO_2 NR/CN NS composites. (d) The PL spectra of CN NS and TiO_2 NR/CN NS composites.

synthesized by introducing the g-C_3N_4 nanosheets into the synthesis. Fig. 1d shows SEM images of TiO_2 NR/CN NS composites, which exhibit a thin flake morphology, and no aggregated TiO_2 NRs are observed, implying that TiO_2 NR uniformly disperseed on the g-C_3N_4. Fig. 1e and f illustrate the TEM and HR-TEM images of TiO_2 NR/CN NS composites. They clearly show that the TiO_2 NRs are well dispersed on the surface of CN NSs.

Fig. 2a shows the XRD of TiO_2 NR, CN NS, and TiO_2 NR/CN NS composites. As-synthesized CN NS presents a characteristic peak at 13.0° (d = 6.75 Å) corresponding to the (100) plane and 27.8° (d = 3.25 Å) corresponding to the (002) direction, which were assigned to the in-plane structural packing tri-s-triazine units and interlayer stacking (002) peak, respectively [26]. The distance is slightly smaller than the size of the tris-s-triazine unit (ca. 0.73 nm), which presumably can be attributed to the presence of small tilt angularity in the structure [27]. XRD pattern of TiO_2 NRs shows diffraction peaks at 27.4°, 36.1°, and 54.3°, which matches with crystalline rutile phase of TiO_2 (JCPDS No. 21-1276). For the TiO_2 NR/CN NS composites, the XRD pattern clearly shows two sets of diffraction peaks, indicating that the composites are composed of TiO_2 and CN. Fig. 2b exhibits the N_2 adsorption-desorption isotherm curves. All of these curves a exhibit type IV isotherm, which confirms the presence of mesopores and macropores. There exists a loop at the middle relative pressure (P/P_0) from 0.4 to 0.6, indicating the presence of the mesopores (Fig. S1 online). The isotherm of g-C_3N_4 displays the highest adsorption at the high relative pressure (P/P_0) near 1, indicating the coexistence of large macropores. The TiO_2 NR/CN NS composites exhibit the loops at both middle and high $P/P_{0,}$ implying the existence of both mesopores and macropores. Correspondingly, the pore size distribution curve (inset in Fig. 2b) exhibits a peak at 3.43 nm, which is attributed to the ultrafine TiO_2 NR stacking holes for TiO_2 NRs. The other broad peak centered at 61.1 nm is probably formed from gaps between entangled CN NSs. The corresponding BET surface areas are 312.3, 110.2, and 241.5 m^2/g for TiO_2 NRs, CN NSs, and TiO_2 NR/CN NSs, respectively. Fig. 2c presents the UV–vis diffuse reflectance spectra (DRS UV–vis) for TiO_2 NR, CN NS, and their composites. Pure TiO_2 NRs exhibit an absorption band edge at 410 nm, indicating an optical band gap of ~3.2 eV, which matches with bulk rutile TiO_2 (~3.2 eV). CN NSs show the absorption band edge at 433 nm, corresponding to an optical band gap of ~2.7 eV, which is slightly lower than the bulk g-C_3N_4 (~2.7 eV) due to the quantum confinement. The TiO_2 incorporation results in a slight shift of the absorption band edge towards blue to 428 nm (~2.9 eV), which may be attributed to the TiO_2 incorporation, resulting in dissociation of g-C_3N_4. Fig. 2d displays the PL spectra of g-C_3N_4 and TiO_2 NR/CN NS composites under excitation at 320 nm. It shows that the PL intensity of g-C_3N_4 greatly decreases after forming the composites, indicating that TiO_2 NR/CN NS composites significantly suppress charge recombination and enhance the charge transfer of the photogenerated electron to TiO_2.

To further investigate the charge transfer process in the TiO_2 NR/CN NS composites, photocurrent and EIS measurements were carried out. Fig. 3a presents the transient photocurrent response to light. The transient photocurrent density of the TiO_2 NR/CN NS is higher than 0.97 μA/cm^2, whereas that of CN NS is 0.56 μA/cm^2, and that of TiO_2 NR is 0.31 μA/cm^2. These results confirm that TiO_2 NR/CN NS composites possess a charge separation that is higher than any single component, which agrees with the PL spectra results. Fig. 3b illustrates the impedance spectra of TiO_2 NRs, CN NSs, and TiO_2 NR/CN NSs under dark and light irradiation (AM 1.5). In the Nyquist diagram, the semicircle is related to the charge transfer behavior at the electrode/electrolyte interface. The smaller the radius, the lower the charge transfer resistance for the corresponding electrode/electrolyte [28]. The Nyquist diagram clearly presents semicircle with a smaller circle under light illumination than in the dark even though the potential of the film is the same, indicating that light promotes the charge transfer. The corresponding equivalent circuit and resistance value are presented in Fig. S2 (online) and Table S1 (online). In the model, R_s denotes the series resistance, which includes the sheet resistance of the transparent conductive oxide (TCO) glass and the external contact resistance of the cell (e.g., wire connections). The parallel R_p and CPE elements characterize the charge transfer resistance and the double layer capacitance in the semiconductor, respectively. In the dark, there is only an equilibrium of charges and consequent electron accumulation in the electrodes, responsible for the higher charge transfer resistances. Under light illustration, electrons are able to flow to the external circuit due to the photoexcitation of the conduction band electrons, which is related to the lower charge transfer resistance. The R_p of TiO_2, CN NSs and TiO_2 NR/CN NSs exhibit the decreasing trend, indicating that the charge separation efficiency increases with decreasing R_p. The TiO_2 NR/CN NS show the smallest arc in all the samples, illustrating that there is an effective charge transfer between the electrode and electrolyte owing to the heterojunction in the composites.

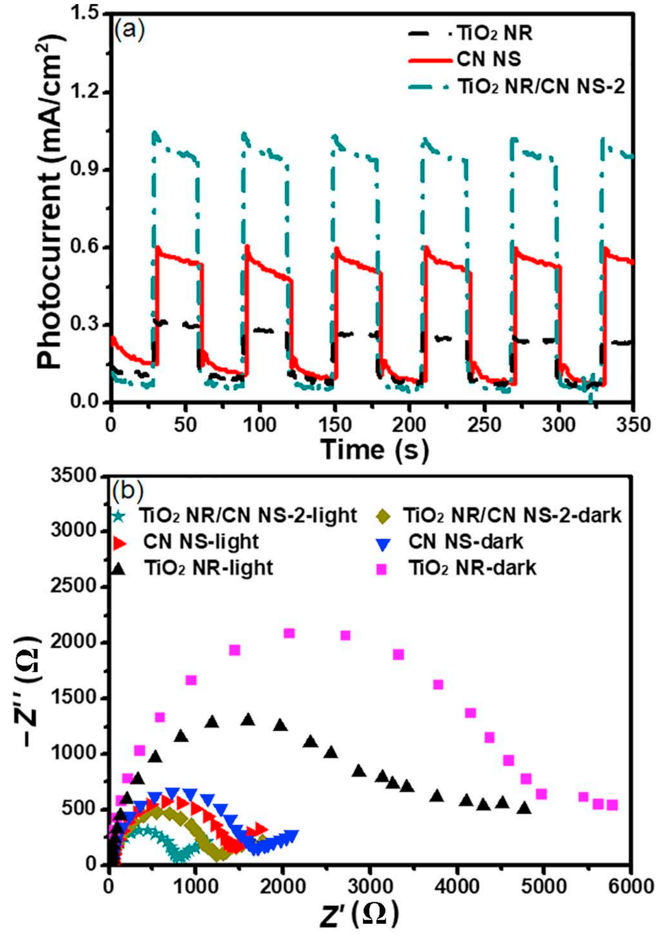

Fig. 3. (Color online) (a) Transient photocurrents measurement of TiO_2 NR, CN NS, and TiO_2 NR/CN NS-2 composites. (b) The EIS spectra of TiO_2 NR, CN NS, and TiO_2 NR/CN NS-2 composites with/without light irradiation.

The photocatalytic activities of samples were evaluated by degradation of RhB and phenol in aqueous solution under both full-spectrum and visible light irradiation. Fig. 4a shows the RhB concentration change in the presence of the different photocatalysts under the full-spectrum light. The concentration of RhB slightly decreases in the absence of photocatalyst due to self-decomposition. The concentration of RhB decreases to ~70%, ~44%, and ~18% within 12 min for P25 TiO_2, TiO_2 NRs and CN NSs,

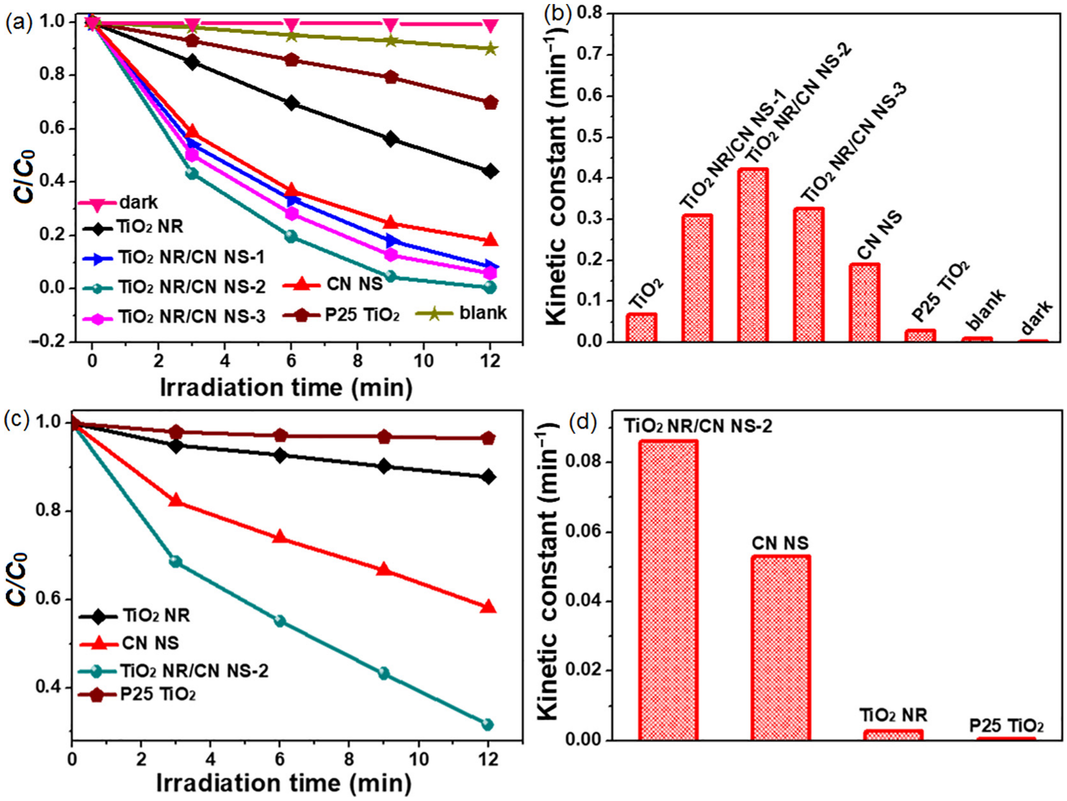

Fig. 4. (Color online) Photocatalytic performance of different photocatalysts. (a) RhB concentration change in the different photocatalysts under the full spectrum light. (b) Their kinetic constant of RhB degradation (*K*). (c) RhB concentration change in the TiO_2 NR, CN NS and TiO_2 NR/CN NS-2 and P25 TiO_2 under the visible light. (d) Their kinetic constant of RhB degradation (*K*).

respectively. During the same time period, the RhB concentration reaches to ~9%, 0.1% and 6% for TiO_2 NR/CN NS-1, 2, 3, respectively. The enhanced photocatalytic activity is observed in the heterojunction TiO_2 NR/CN NS composites. The kinetic constant of RhB degradation (*K*), which is shown in Fig. 4b, could directly stand for the photocatalytic activity of photocatalyst. The *K* of pure TiO_2 NRs is about 0.068 min^{-1}, which is about 2-fold higher than P25 TiO_2 (0.029 min^{-1}), and this is attributed to the high surface area for TiO_2 NRs. The CN NRs exhibit a much higher *K* value (0.191 min^{-1}), indicating that g-C_3N_4 has stronger activity as compared to TiO_2. In the case of a heterojunction catalyst of TiO_2 NR/CN NSs, all the composites exhibited higher *K* value as compared to TiO_2 NR and CN NSs. The TiO_2 NR/CN NS-2 heterojunction catalyst exhibited the highest photocatalytic activity ($K = 0.421$ min^{-1}), which was approximately 6- and 15-fold higher than TiO_2 NR and P25 TiO_2, respectively. The visible light photocatalytic activity was also characterized under visible light irradiation ($\lambda > 420$ nm), as shown in Fig. 4c and d. The concentration of RhB was maintained at a nearly constant level, indicating P25 TiO_2 possesses no visible light photocatalytic activity. However, the TiO_2 NRs showed relatively weak photocatalytic activity due to thepossibility that the TiO_2 NRs may be sensitized by RhB. CN NRs exhibited photocatalytic activity in the visible light region because they have a narrow band gap (~2.7 eV) and visible light absorbance. The TiO_2 NR/CN NR-2 exhibited relatively high photocatalytic activity. The *K* value of RhB degradation under visible light is approximately 0.086 min^{-1}, which is higher than that of P25 TiO_2 and TiO_2 NR under full-spectrum light. The photocatalytic activity of TiO_2 can be further enhanced by the formation of a heterojunction with g-C_3N_4 nanosheets due to the formation of the heterojunction.

Furthermore, phenol, as an undegradable organic molecule, was also employed to investigate the photocatalytic activity of the as-prepared catalysts. Fig. 5a and b show the phenol decomposition in aqueous dispersion of TiO_2 NRs, CN NSs and TiO_2 NR/CN NS-2 under full-spectrum light and visible light, respectively. The *K* value for phenol degradation is much smaller than that of RhB, indicating that it is more difficult to degrade phenol than RhB. The *K* value of TiO_2 NR/CN NS-2 is approximately 9 and 2 times higher than that of TiO_2 NR and CN NSs, respectively. Similar results were observed during the visible light photocatalytic degradation. To further test the mineralization degree of phenol during the photodegradation process, the evolution of total organic compounds during light irradiation was investigated (Fig. 5c). Approximately 84% of phenol was mineralized to CO_2 within 160 min with the TiO_2 NR/CN NS-2, which is 4.78 and 1.8 times higher than that obtained with the TiO_2 NRs and CN NSs during the same period, respectively. This result indicates that the TiO_2 NR/CN NS-2 has a much higher mineralization efficiency for the photodegradation of phenol than TiO_2 NR and CN NS, respectively. In addition, photostability is another key factor for the practical application. Fig. 5d shows the recycling of TiO_2 NR/CN NS-2 for the RhB degradation. Over three consecutive cycles, no obvious deactivation of the photocatalyst was observed, indicating that the composite catalyst TiO_2 NR/CN NS possesses excellent stability for the photocatalytic reaction.

Superoxide anion radical ($^{\cdot}O_2^-$), singlet oxygen ($^1O_2$), hydrogen peroxide (H_2O_2), hydroxyl radical ($^{\cdot}OH$), and hole are well known as intrinsic reactive oxygen species (ROS) produced at the surfaces of TiO_2 by adsorbed O_2 or H_2O in the photocatalysis process [10]. Superoxide anion radical is generated from adsorbed O_2 and photogenerated electron. Recently, Huang and co-workers [29–31] demonstrated the strong oxidative capability of superoxide radicals. They can oxidize various organic contaminants such as phenol, bisphenol A, and other stubborn pollution, and can further convert into singlet oxygen through an oxidation process or H_2O_2 through reduction. Hydroxyl radical is generated by the

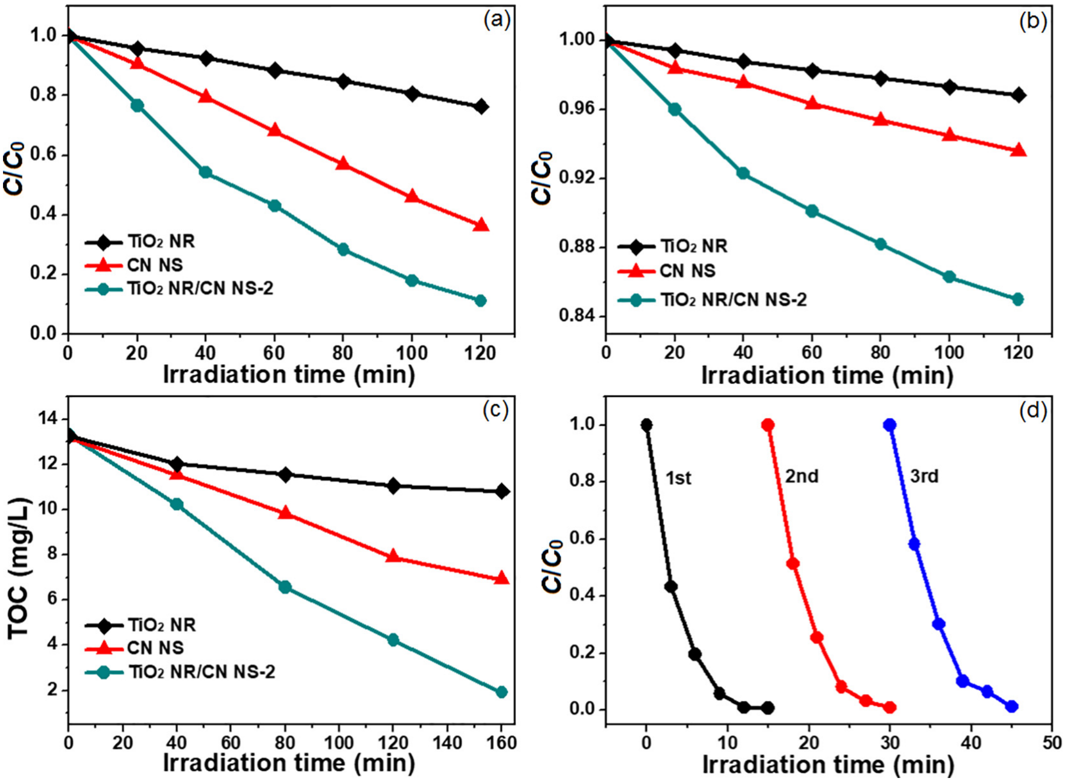

Fig. 5. (Color online) Photocatalytic performance of different photocatalysts. The phenol decomposition in TiO_2 NR, CN NS and TiO_2 NR/CN NS-2 composites aqueous dispersion under full spectrum light (a) and visible light (b). (c) Temporal evolution of total organic compound concentration in TiO_2 NR, CN NS and TiO_2 NR/CN NS-2 composites. (d) Cycling test of the RhB degradation for TiO_2 NR/CN NS-2 composites.

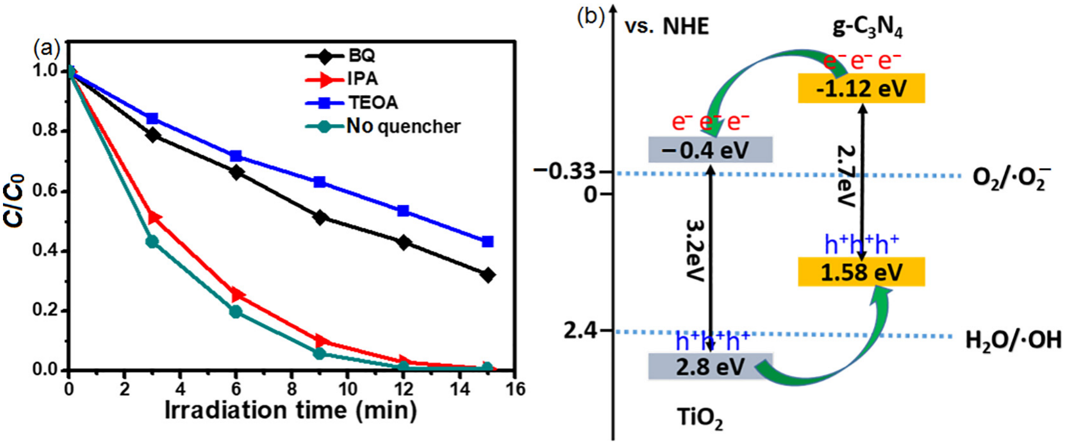

Fig. 6. (Color online) (a) Photodegradation efficiency of the RhB with different trapping agent (BQ, $^{\cdot}O_2^-$); (IPA, $^{\cdot}OH$); (TEOA, h^+). (b) Photocatalytic mechanism of the TiO_2 NR/CN NS-2 composites.

photocatalytic oxidization of adsorbed H_2O at the surface with holes at valance band and produces $^{\cdot}OH$, which is dimerized to H_2O_2. To elucidate the active ROS and photocatalytic mechanism in the TiO_2 NR/CN NS composite catalyst, radical and hole quenching experiments were carried out by monitoring the degradation of RhB in the presence of a different scavenger. Figs. 6a and S3 (online) illustrate the effect of various scavengers on the kinetic constant of photocatalytic degradation of RhB by adding isopropanol (IPA), benzoquinone (BQ), or triethanolamine (TEOA) scavenger. The kinetic constant is 0.36 min^{-1} without any scavenger. The addition of isopropanol as a hydroxyl radical scavenger slightly inhibits the degradation of RhB, with an approximately 8% reduction of reaction rate, which indicates that $^{\cdot}OH$ slightly contributes to the degradation of RhB. The injecting of BQ (as the superoxide anion radical scavenger) or TEOA (a scavenger for the hole) retard the reaction rate by ~80% and ~86%, respectively. This reduction in reaction rate indicates that both the superoxide anion radical and photogenerated hole are dominant active species in the TiO_2 NR/CN NS photocatalytic degradation process. According to previous reports [32–35], the active species of TiO_2 are superoxide anion radical and hydroxyl radical in the photodegradation of organic molecules. The main contributors of g-C_3N_4 are superoxide anion radical and holes in the photocatalytic decomposition [27,36]. Combining with the main contributors are super anion radical and holes, and we can speculate that the holes can mainly transfer from TiO_2 to g-C_3N_4 and not produce hydroxyl radical in the TiO_2 NR/CN NS composites. On the basis of the charge transfer of the TiO_2 NR/CN NS heterojunction and the above quenching experiment, we propose a possible photocatalytic mechanism (Fig. 6b). Fig. S4 (online) illustrates that the optical band gap of TiO_2 NR is ~3.2 eV, which is larger than that of bulk rutile TiO_2 (~3.0 eV), due to the ultrafine particle size of TiO_2 NRs. The optical band gap of CN NSs is ~2.7 eV. Due to the band alignment and potential difference, the photogenerated electrons at the CB of CN NSs can quickly transfer to the CB of TiO_2 NRs. The electrons further reduce the adsorbed oxygen and form superoxide anion radical, which is the active species for the degradation of RhB. The photo-induced holes rapidly transfer to the VB of CN NSs (1.58 eV vs. NHE), which cannot form hydroxyl radical due to the more negative potential as compared to the potential of $^{\cdot}OH/OH^-$ (1.99 eV vs. NHE). The holes at the VB of CN NSs may directly react with RhB. Additionally, the TiO_2 NR effectively trap electrons at their CB, and the holes are stored at the VB of CN NSs, spatially separating electron-hole pairs, which further promotes the degradation of organic molecules.

4. Conclusions

We demonstrated a simple method to fabricate an ultrafine TiO_2 NR/CN NS hybrid photocatalyst by one-step hydrothermal route. The as-prepared catalyst exhibits a large surface area and good charge-separation efficiency, and possesses extremely high performance for photocatalytic degradation. Under visible light ($\lambda > 420$ nm) irradiation, the apparent rate of the heterojunction of TiO_2 NR/CN NR is 172 and 41 times higher than that of the P25 TiO_2 and TiO_2 NRs, respectively. We demonstrated that the superoxide anion radical and holes are the dominant active species in the photocatalytic degradation of organic molecules.

Conflict of interest

The authors declare that they have no conflict of interest.

Acknowledgments

This work was supported by the Beijing Municipal High Level Innovative Team Building Program (IDHT20180504), the National Natural Science Foundation of China (21671011), Beijing High Talent Program and Beijing Natural Science Foundation (KZ201710005002). The authors thank the Large-scale Instrument and Equipment Platform of Beijing University of Technology, China Postdoctoral Science Foundation, and Beijing Postdoctoral Research Foundation.

Appendix A. Supplementary data

Supplementary data associated with this article can be found, in the online version, at https://doi.org/10.1016/j.scib.2018.04.002.

References

[1] Asahi R, Morikawa T, Ohwaki T, et al. Visible-light photocatalysis in nitrogen-doped titanium oxides. Science 2001;293:269–71.

[2] Asahi R, Morikawa T, Irie H, et al. Nitrogen-doped titanium dioxide as visible-light-sensitive photocatalyst: designs, developments, and prospects. Chem Rev 2014;114:9824–52.

[3] Hoffmann MR, Martin ST, Choi W, et al. Environmental applications of semiconductor photocatalysis. Chem Rev 1995;95:69–96.

[4] Huang H, Cao R, Yu S, et al. Single-unit-cell layer established Bi_2WO_6 3D hierarchical architectures: efficient adsorption, photocatalysis and dye-sensitized photoelectrochemical performance. Appl Catal B Environ 2017;219:526–37.

[5] Huang H, Xiao K, He Y, et al. In situ assembly of BiOI@$Bi_{12}O_{17}Cl_2$ p-n junction: charge induced unique front-lateral surfaces coupling heterostructure with high exposure of BiOI 001 active facets for robust and nonselective photocatalysis. Appl Catal B Environ 2016;199:75–86.

[6] Hurum DC, Agrios AG, Gray KA, et al. Explaining the enhanced photocatalytic activity of degussa P25 mixed-phase TiO_2 using EPR. J Phys Chem B 2003;107:4545–9.

[7] Schmidt CM, Weitz E, Geiger FM. Interaction of the indoor air pollutant acetone with degussa P25 TiO_2 studied by chemical ionization mass spectrometry. Langmuir 2006;22:9642–50.

[8] Lang X, Ma W, Chen C, et al. Selective aerobic oxidation mediated by TiO_2 photocatalysis. Acc Chem Res 2013;47:355–63.

[9] Ma Y, Wang X, Jia Y, et al. Titanium dioxide-based nanomaterials for photocatalytic fuel generations. Chem Rev 2014;114:9987–10043.

[10] Nosaka Y, Nosaka AY. Generation and detection of reactive oxygen species in photocatalysis. Chem Rev 2017;117:11302–36.

[11] Low J, Yu J, Jaroniec M, et al. Heterojunction photocatalysts. Adv Mater 2017;29:1601694.

[12] An X, Wang Y, Lin J, et al. Heterojunction: important strategy for constructing composite photocatalysts. Sci Bull 2017;62:599–601.

[13] Fu J, Yu J, Jiang C, et al. g-C_3N_4-based heterostructured photocatalysts. Adv Energy Mater 2018;8:1701503.

[14] Wang X, Maeda K, Thomas A, et al. A metal-free polymeric photocatalyst for hydrogen production from water under visible light. Nat Mater 2009;8:76–80.

[15] Ong WJ, Tan LL, Ng YH, et al. Graphitic carbon nitride (g-C_3N_4)-based photocatalysts for artificial photosynthesis and environmental remediation: are we a step closer to achieving sustainability? Chem Rev 2016;116:7159–329.

[16] Wen J, Xie J, Chen X, et al. A review on g-C_3N_4-based photocatalysts. Appl Surf Sci 2017;391:72–123.

[17] Lin Z, Wang X. Nanostructure engineering and doping of conjugated carbon nitride semiconductors for hydrogen photosynthesis. Angew Chem Int Ed 2013;52:1735–8.

[18] Wang Y, Yao J, Li H, et al. Highly selective hydrogenation of phenol and derivatives over a Pd@carbon nitride catalyst in aqueous media. J Am Chem Soc 2011;133:2362–5.

[19] Jiang Z, Zhu C, Wan W, et al. Constructing graphite-like carbon nitride modified hierarchical yolk-shell TiO_2 spheres for water pollution treatment and hydrogen production. J Mater Chem A 2016;4:1806–18.

[20] Li Y, Wang J, Yang Y, et al. Seed-induced growing various TiO_2 nanostructures on g-C_3N_4 nanosheets with much enhanced photocatalytic activity under visible light. J Hazard Mater 2015;292:79–89.

[21] Li K, Gao S, Wang Q, et al. In-situ-reduced synthesis of Ti^{3+} self-doped TiO_2/g-C_3N_4 heterojunctions with high photocatalytic performance under led light irradiation. ACS Appl Mater Interfaces 2015;7:9023–30.

[22] Hao R, Wang G, Tang H, et al. Template-free preparation of macro/mesoporous g-C_3N_4/TiO_2 heterojunction photocatalysts with enhanced visible light photocatalytic activity. Appl Catal B Environ 2016;187:47–58.

[23] Yang C, Qin J, Xue Z, et al. Rational design of carbon-doped TiO_2 modified g-C_3N_4 via in-situ heat treatment for drastically improved photocatalytic hydrogen with excellent photostability. Nano Energy 2017;41:1–9.

[24] Tong Z, Yang D, Xiao T, et al. Biomimetic fabrication of g-C_3N_4/TiO_2 nanosheets with enhanced photocatalytic activity toward organic pollutant degradation. Chem Eng J 2015;260:117–25.

[25] Xiang G, Wang YG, Wu D, et al. Size-dependent surface activity of rutile and anatase TiO_2 nanocrystals: facile surface modification and enhanced photocatalytic performance. Chem Eur J 2012;18:4759–65.

[26] Wang Y, Wang X, Antonietti M. Polymeric graphitic carbon nitride as a heterogeneous organocatalyst: from photochemistry to multipurpose catalysis to sustainable chemistry. Angew Chem Int Ed 2012;51:68–89.

[27] Yan S, Li Z, Zou Z. Photodegradation of rhodamine B and methyl orange over boron-doped g-C_3N_4 under visible light irradiation. Langmuir 2010;26:3894–901.

[28] Hou Y, Wen Z, Cui S, et al. Constructing 2D porous graphitic C_3N_4 nanosheets/nitrogen-doped graphene/layered MoS_2 ternary nanojunction with enhanced photoelectrochemical activity. Adv Mater 2013;25:6291–7.

[29] Huang H, Li X, Wang J, et al. Anionic group self-doping as a promising strategy: band-gap engineering and multi-functional applications of high-performance CO_3^{2-}-doped $Bi_2O_2CO_3$. ACS Catal 2015;5:4094–103.

[30] Huang H, He Y, Li X, et al. $Bi_2O_2(OH)(NO_3)$ as a desirable $[Bi_2O_2]^{2+}$ layered photocatalyst: strong intrinsic polarity, rational band structure and 001 active facets co-beneficial for robust photooxidation capability. J Mater Chem A 2015;3:24547–56.

[31] Huang H, Tu S, Zeng C, et al. Macroscopic polarization enhancement promoting photo- and piezoelectric-induced charge separation and molecular oxygen activation. Angew Chem Int Ed 2017;56:11860–4.

[32] Dong F, Zhao W, Wu Z, et al. Band structure and visible light photocatalytic activity of multi-type nitrogen doped TiO_2 nanoparticles prepared by thermal decomposition. J Hazard Mater 2009;162:763–70.

[33] Turchi CS, Ollis DF. Photocatalytic degradation of organic water contaminants: mechanisms involving hydroxyl radical attack. J Catal 1990;122:178–92.

[34] Ishibashi KI, Fujishima A, Watanabe T, et al. Detection of active oxidative species in TiO_2 photocatalysis using the fluorescence technique. Electrochem Commun 2000;2:207–10.

[35] Linsebigler AL, Lu G, Yates JT. Photocatalysis on TiO_2 surfaces: principles, mechanisms, and selected results. Chem Rev 1995;95:735–58.

[36] Dong G, Zhang L. Porous structure dependent photoreactivity of graphitic carbon nitride under visible light. J Mater Chem 2012;22:1160–6.

Shiliang Luan received his B.S. from Yanching Institute of Technology in 2014. He is a M.S. candidate in the department of Chemistry and Chemical Engineering, Beijing University of Technology. His current research interest is TiO_2 based photocatalysts.

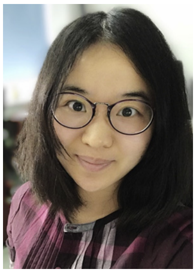

Dan Qu received her B.S. in polymer material and engineering from College of Chemistry, Jilin University in 2012 and Ph.D. in condensed matter physics from Changchun Institute of Optics, Fine Mechanics and Physics, Chinese Academy of Sciences in 2017 under the supervision of Prof. Zaicheng Sun. Currently, she is working at Beijing University of Technology. Her research interests include the controlled synthesis of fluorescent carbon dots and their applications.

Zaicheng Sun received his Ph.D. in Changchun Institute of Applied Chemistry, Chinese Academy of Sciences in 1999. He was an AvH Research Fellow in 2001. After a few years Postdoctoral Fellow at Max-Planck Institute for Polymer Research, University of Washington; University of Delaware and University of New Mexico. He joined in the Changchun Institute of Optics, Fine Mechanics and Physics, Chinese Academy of Science. In 2016, he joined in Beijing University of Technology. His research interests are highly efficient photocatalyst with visible light response and the synthesis and applications of fluorescent carbon dots.